Supporting Information

Energy-Looping Nanoparticles: Harnessing Excited State Absorption for Deep-Tissue Imaging

Elizabeth S. Levy,[1‡] Cheryl A. Tajon,[1‡] Thomas S. Bischof,[1] Jillian Iafrati,[2] Angel Fernandez-Bravo,[1] David Garfield,[1,3] Maysamreza Chamanzar,[4°] Michel M. Maharbiz,[4] Vikaas S. Sohal,[2] P. James Schuck,[1] Bruce E. Cohen,[1] and Emory M. Chan[,1]*

The Molecular Foundry, Lawrence Berkeley National Laboratory, Berkeley, CA 94720

[*] To whom correspondence should be addressed. E-mail: EMChan@lbl.gov
[‡] These authors contributed equally to this work.

[1]The Molecular Foundry, Lawrence Berkeley National Laboratory, Berkeley, CA 94720
[2]Department of Psychiatry, University of California, San Francisco, CA 94143
[3]Department of Chemistry, University of California, Berkeley, CA 94720
[4]Department of Electrical Engineering and Computer Science, University of California, Berkeley, CA 94720
[°]*Present address:* Department of Electrical and Computer Engineering, Carnegie Mellon University, Pittsburgh, PA 15213 USA

Table of Contents

1. Experimental materials and methods.

Materials. Sodium trifluoroacetate, sodium oleate, ammonium fluoride, lanthanide chlorides (anhydrous, 99.9+%), oleic acid (OA) (90%), 1-octadecene (ODE) (90%), agarose, Intralipid (IL), 5-μm polystyrene (PS) beads (10% w/v), and phosphate buffer saline (PBS) were purchased from Sigma. Paraformaldehyde was purchased from Electron Microscopy Science.

Synthesis of core and core/shell ELNPs. $NaYF_4$:20% Gd^{3+}, Tm^{3+} particles with diameter d = 11 ± 1 nm were synthesized based on reported procedures[1] and optimized using the Workstation for Automated Nanocrystal Discovery and Analysis (WANDA), a high-throughput robot at the Molecular Foundry.[2] Tm^{3+} was doped from 0.1 to 1.5 atomic percent relative to the total rare earth content (Y, Gd, Tm). Lanthanide ion stock solutions were prepared with lanthanide chlorides in oleic acid and 1-octadecene. Yttrium oleate (0.1 M) was prepared in 1:1 w/w OA/ODE, gadolinium oleate (0.2 M) was prepared in 1:1.33 w/w OA/ODE, and thulium oleate (0.0048 M) was prepared in 1:2 w/w OA/ODE. To form the lanthanide oleates, the lanthanide chlorides, OA, and ODE were added to a round-bottom flask and then heated at 110 °C under vacuum. The solutions were pumped with vacuum and purged with nitrogen three times until all solid had dissolved, for a total of ca. 30 min under vacuum. Stock solutions were stored in a nitrogen-filled glovebox.

A typical reaction contained 400 μmol total lanthanide consisting of 80 μmol Gd^{3+}, 3.2 μmol Tm^{3+}, and 316.8 μmol Y^{3+}. In addition to the lanthanides, 2 mmol ammonium fluoride, 1.25 mmol sodium oleate, 11.50 mmol OA, and 22.17 mmol ODE were added to a 40 mL reaction vial with two rare-earth-magnetic stir bars. In WANDA, the reaction vials were heated to 315 °C at 30 °C/s, allowed to react at temperature for 45 minutes, and then cooled rapidly with nitrogen gas flow. WANDA is enclosed in a glovebox, allowing for dry and oxygen-free reaction conditions.

To isolate the nanoparticles, ethanol was added to the solution and the nanoparticles were isolated by centrifugation (5 min at 4000 rpm). The pellet was suspended in hexanes and centrifuged to remove large and aggregated particles. The nanoparticles were washed two additional times by adding ethanol, isolating by centrifugation, and dissolving the pellet in hexanes. The nanoparticles were stored in hexanes.

Shell growth. A two-nanometer thick $NaGdF_4$ shell was grown on selected ELNP cores using a layer-by-layer protocol modified from Li et al[3] and adapted for WANDA as described in Mehra et al.[4] Briefly, 6 mL ODE and 4 mL OA were added to the dried ELNP cores and heated to 275 °C in the WANDA glove box. The automated protocol alternated between injections of a 0.2 M sodium trifluoroacetate in OA/ODE (25% v/v) solution and a 0.2 M gadolinium oleate solution in OA/ODE (40% v/v) in a 2:1 mole ratio of sodium to gadolinium precursor. One injection was performed every 15 minutes for a total of 12 injections (6 injections for each precursor). Following the last injection, each reaction was heated at 275 °C for an additional 30 minutes and then cooled by nitrogen flow. Core-shell $NaYF_4$ nanoparticles doped with Nd^{3+}/Yb^{3+}/Ho^{3+}/Gd^{3+} (20/10/2/20 at %) were synthesized using analogous methods.

Nanoparticle characterization. TEM was performed using a Zeiss Libra 120 microscope at 120 kV acceleration. Size statistics were acquired for approximately 100 nanoparticles using ImageJ software. X-Ray diffraction (XRD) measurement was performed using a Bruker D8 Discover diffractometer with Cu Kα radiation. Dynamic light scattering was performed on a Malvern Zetasizer Nano instrument.

Loading NPs into polystyrene beads. Core-shell NPs were loaded into microbeads[5] (*d* = 5 μm; Sigma-Aldrich) by swelling 0.5 mg of PS beads with 250 μL of an 5% (*v/v*) chloroform solution in butanol. ELNPs (2 mg in 15 μL of hexane) were added to the bead suspension, followed by brief vortexing. After stagnant incubation at 25 °C for 4 hours, the beads were washed four times total, alternating between ethanol and cyclohexane. At the end of each wash step, the particles were centrifuged at 3000 rpm (4200 g) for four minutes, except for the last wash, which used 1100 rpm (1500 g) for two minutes.

Ligand removal. ELNPs were rendered hydrophilic using a procedure modified from Bogdan et al.[6] ELNPs in hexanes were dried in a vial under N_2 flow and dispersed in 40 mM HCl in 80% ethanol (pH = 1.4) to give a 1 mg/mL dispersion. After 30 min sonication, 1 mL of deionized water was added to the solution and extracted twice against 1.5 mL of diethyl ether. Trace diethyl ether in the aqueous layer was removed with a gentle N_2 flow. The water-dispersible ELNPs were washed with water in a 30 KDa centrifugal filter (Millipore) at 3000 x *g*, and 120 μL of ligand-free ELNPs were retained in the filter at ca. 10 mg/mL.

Cell culture and microscopy of fixed cells. HeLa cells were maintained in DMEM (Sigma-Aldrich), 10% FBS (Gibco), and 1 x penicillin/streptomycin (Sigma-Aldrich) at 37 °C and 5% CO_2. Ibidi μ-Slide VI $^{0.4}$ chambers were coated with 30 μL of 0.2 mg/mL fibronectin (MP Biomedicals) in Dulbecco's phosphate buffered saline with 0.133 g/L $CaCl_2$ and 0.1 g/L $MgCl_2$ (D-PBS, Sigma-Aldrich, #D8662) to give a 10 μg/cm^2 coating density. Following 20 min incubation at room temperature, chambers were washed twice with 150 μL of D-PBS with $CaCl_2$ and $MgCl_2$. Chambers were seeded with 3000 HeLa cells/cm^2 and allowed to attach for 1.5 h at 37 °C in 5% CO_2. Media was carefully removed and replaced with 30 μL of the following reagents in complete DMEM media: ca. 140 nM ELNPs (9% v/v added ELNP dispersion) or vehicle control. ELNP and vehicle solutions in media were filter sterilized using a 0.22-μm syringe filter (Pall) before treatment of the cells. After a 17-h incubation at 37°C in 5% CO_2, cells were washed two times with 150 μL D-PBS with $CaCl_2$ and $MgCl_2$. Cells were then fixed with 3.7% formaldehyde (Sigma-Aldrich) in D-PBS with $CaCl_2$ and $MgCl_2$, incubated for 20 min at RT, and washed twice with 150 μL of D-PBS with $CaCl_2$ and $MgCl_2$. Cells were imaged with a 1064 nm laser (10^6 W/cm^2) and 50x objective (0.75 NA) with a 50-μm pinhole with 0.5 sec acquisition time per pixel at 0.5 μm resolution.

Preparation of phantoms. Intralipid (0.1-0.5% w/v) was added to a hot solution of agarose in deionized water (1% *w/v*). Phantoms 0.5-2 mm in thickness were cast between two coverslips separated by spacers of known height. The molten agarose mixtures were injected into these molds and allowed to solidify for 20 minutes.

Preparation of mouse brain tissue. Animal tissue experiments were performed in accordance with protocols approved by Administrative Panels on Laboratory Animal Care at the University of California, San Francisco and by an Animal Welfare Protocol approved by Lawrence Berkeley National Laboratory. Brain slices were prepared as described previously.[7] Briefly, adult C57BL/6 mice (7-10 weeks old) were anesthetized with

isofluorane and decapitated. Using a vibratome (Leica VT1200 S), coronal brain slices were prepared at different thicknesses (ranging from 0.5 and 1 mm, reported before fixation) in a chilled slicing solution consisting of 234 mM sucrose, 11 mM glucose, 24 mM $NaHCO_3$, 2.5 mM KCl, 1.25 mM NaH_2PO_4, 10 mM $MgSO_4$, and 0.5 mM CaCl. Slices were then fixed overnight in 4% paraformaldehyde/1X PBS then mounted on glass coverslips with a glycerol-based medium (Vectashield, Vector laboratories). Mouse brain transmission spectra were recorded with a collimated beam using an ASD QualitySpec Pro Vis/NIR absorption spectrometer.

Confocal microscopy and spectroscopy. UCNP emission measurements were performed using a Horiba Jobin Yvon LabRAM ARAMIS confocal microscope with filters purchased from Semrock. ELNPs were excited with a 1064 nm continuous-wave laser (MPC) filtered with a 1064 nm laser-line (LL) filter and 980 nm long-pass filter. An 890-nm short pass (SP) filter was used both as a dichroic mirror and as an emission filter. For emission maps of ELNPs, the 800 nm emission peak was integrated between 740 and 870 nm. $NaYF_4$: Nd^{3+}/Yb^{3+}/Ho^{3+}/Gd^{3+} (20/10/2/20 at %) UCNPs with undoped shells were imaged with a 785-nm laser (LaserQuantum) at 10^6 W/cm^2 with spectral acquisition from 450 to 700 nm. The laser was filtered with 785 nm LL filter (Semrock). A 785 nm SP filter was the dichroic mirror and emission filter. The 540 and 640 nm emission peaks were integrated across ranges of 530-560 nm and 625-675 nm, respectively. Spectral intensities were corrected for the wavelength-dependent instrumental response using a calibrated lamp (Avantes). Average excitation power densities were calculated using measured laser powers and using the $1/e^2$ area calculated from the reflection of the laser spot.

Imaging through phantoms and brain slices. ELNP-loaded beads dispersed in ethanol were drop-cast on a silicon substrate. A spacer (2 mm) was used to separate the substrate from the coverslip under which the phantom sample or brain tissue sample were affixed. This geometry allowed for imaging of the identical microparticles under different samples. ELNP emission was mapped through phantoms of thickness from 1 to 2 mm, IL concentrations from 0.1% to 0.5%, and brain tissue 0.5 and 1 mm thick. XY maps were acquired with resolution of 0.5-1.0 μm with a 200-μm pinhole, and imaged with a 50X 0.5NA objective (Olympus). Integration times ranged from 0.1 to 2 seconds.

Image analysis. To compare the intensities of ELNP and UCNP-loaded microbeads, luminescence micrographs were analyzed in ImageJ. Following background subtraction, the integrated intensity of each bead was measured in a circular region of interest around the bead. The signal retention ratio of the phantoms, $S_{phantom}/S_0$, was calculated by dividing the integrated intensity of bead luminescence, $S_{phantom}$, measured through the phantom by the intensity S_0 measured without the phantom.

Upconversion luminescence of Tm^{3+} concentration series. A library of $NaYF_4$:20% Gd^{3+}, X% Tm^{3+} was synthesized with X = (0.1 to 1.5%). To compare intensities and eliminate size effects, nanoparticles were synthesized with similar diameters (d = 11±1 nm). 100 μl of each ELNP in hexane (15 mg/ml) was deposited into three different wells of a white round-bottom polypropylene microplate (96 wells, Corning). The actual Tm^{3+} loading and mass loading of the ELNP solutions were verified by inductively coupled plasma – optical emission spectroscopy (ICP-OES). The hexane solutions were allowed to evaporate for 30 minutes under ambient conditions, after which the microplates were covered loosely and centrifuged at 3500 rpm for 10 min to compress and center each pellet in the bottom of its well. The pellets were dried overnight under vacuum before optical

measurements. Upconversion intensities were measured with confocal luminescence microscopy at 10^5 W/cm^2 through a 20x 0.25NA objective (Olympus). Integrated intensities (750-870 nm) were averaged across the three replicate wells.

Live cell imaging. HeLa cells were maintained in L-15 (Sigma-Aldrich), 10% FBS (Gibco), and 1x penicillin/streptomycin (Sigma-Aldrich) at 37 °C. Ibidi µ-Slide I $^{0.4}$ Luer ibiTreat chambers were marked with a razor blade to indicate reference points and coated with fibronectin (MP Biomedicals) at 10 µg/cm^2 coating density. Following 20 min incubation at room temperature, chambers were washed three times with 200 µL of D-PBS with $CaCl_2$ and $MgCl_2$. Chambers were seeded with 3000 HeLa cells/cm^2 and allowed to attach for 1.5 h at 37°C. Media was carefully removed and replaced with 200 µL of ca. 280 nM ELNPs or 1 µM staurosporine (STS). ELNP and STS solutions in media were filter sterilized using a 0.22-µm syringe filter (Pall) before treatment of the cells. After 21 h at 37°C, ELNP-treated cells were washed three times with 200 µL of complete L-15 media. The surfaces of Ibidi chambers were cleaned with 70% EtOH and dried completely. The chamber was inverted over a 12-well plate filled with complete L-15 media. Reservoirs were submerged into media, allowing cells to be positioned closest to the objectives of an upright Horiba LabRAM Aramis Raman microscope. Chambers were taped down to 12-well plate for stability and cell coordinates were recorded relative to internal reference point. Imaging was conducted at RT using a 1064 nm laser and 50x objective (0.75 NA). The pinhole was set to 200 µm and completed with a 0.1 s acquisition time and 0.75×0.75 µm pixel size. The laser excitation shutter was closed during stage movements in between each pixel. The acquisition time (0.1 s) for each pixel was comparable to the time required to close the shutter, move the stage, and open the shutter in between each pixel. Thus the overall acquisition time for a scan was typically three to four times greater than the actual laser exposure time (the number of pixels times the pixel acquisition time). **In this work, the laser exposure times refer only to the time that the cells are exposed to laser radiation**.

Following imaging, cells were stained with 3 µg/mL propidium iodide (PI) in complete L-15 media for 5 min. Cells were washed three times each with 200 µl PBS and with 200 µl D-PBS with $CaCl_2$ and $MgCl_2$. Cells were fixed with 3.7% formaldehyde (Sigma-Aldrich) in D-PBS with $CaCl_2$ and $MgCl_2$, incubated for 20 min at RT, and washed three times with 200 µl D-PBS with $CaCl_2$ and $MgCl_2$. Using the recorded coordinates as a guide, the exact cell exposed to 1064 nm light was readily identified and imaged on an inverted Zeiss LSM 710 confocal microscope using either a 488 nm or 514 nm laser through a 63x oil objective. Zeiss' Lambda Mode was used to collect emission spectra (550-725 nm) on the PI-treated cells with 514 nm excitation, and data points were background subtracted. Cells treated with STS were incubated for 18 h before staining with PI, fixed with formaldehyde, and imaged on the Zeiss confocal microscope. Autofluorescence images were collected in the Zeiss microscope using 488 nm excitation and integrating the emission from 506 to 735 nm.

CellTiter-Glo viability assay. Treated HeLa cells were prepared as described above. After cell attachment, media was replaced with either 40 µL of vehicle, ELNPs at ca. 140 nM, or 1 µM staurosporine (STS, Sigma-Aldrich) in complete DMEM. Solutions were filtered through a 0.22 µm syringe filter before addition to cells. Following a 17-h overnight incubation, 40 µL of CellTiter-Glo reagent (Promega) was added to each chamber. Chambers were tilted intermittently to evenly distribute assay reagent and allowed to sit at

room temperature for 10 min. Chamber contents were collected and transferred to a 96-well solid-white plate (Corning). The luminescence (250-850 nm) of each well was measured between using a Spectra Max Gemini Fluorescence plate reader (Molecular Devices). To rule out interference from ELNPs, the same procedure was repeated on vehicle and ELNP-treated media without the presence of cells. All experimental groups were run in triplicate and data points were blank subtracted. P values were calculated using an unpaired *t* test in GraphPad Prism software.

2. Rate equation simulations

Simulation methods. Kinetic simulations were performed with Igor Pro 6.3 (Wavemetrics) using methods detailed in our previous publications.[8,9] The concentration N_i (in nm^{-3}) of a lanthanide $4f^N$ manifold *i* over time is determined by the incoming and outgoing rates dN_i/dt of electric dipole (ED) and magnetic dipole (MD) radiative transitions, non-radiative multiphonon relaxation (MPR), and energy transfer (ET). Because lanthanide transition rates can vary by 10 or more orders of magnitude, solving differential rate equations for the population of lanthanide manifolds is a stiff problem. Therefore, these ordinary differential equations, which represent the population of each manifold in the simulated system, were solved numerically using the Igor Pro's Backwards Differentiation Formula integration method, which converges more rapidly for stiff problems. All ions were placed in their ground states at the start of the simulation. Time steps for iterations were determined dynamically by the integration algorithm, and all simulated systems reached steady state by the end of the simulation time period. Lifetimes were simulated by performing a second simulation in which the excitation power density was set to zero, and initial manifold populations were set to the steady state populations of the previous simulation.

Emission intensities were simulated by calculating the photon emission rates for each manifold *i*. To determine the most important transitions for a given energy transfer pathway, we considered only transitions with the highest branching ratios (β_{ij}) or contribution ratios (κ_{ij}), where:

$$\beta_{ij,t} = \frac{\left(dN_i/dt\right)^t_{i\to j}}{\sum_{\substack{t=ED,MD,\\ET,MPR}} \sum_m \left(dN_i/dt\right)^t_{i\to m}} \qquad (S1)$$

$$\kappa_{ij,t} = \frac{\left(dN_j/dt\right)^t_{i\to j}}{\sum_t \sum_m \left(dN_j/dt\right)^t_{m\to j}} \qquad (S2)$$

For a given transition type t (ED/MD radiative, ET, MPR) from i to j, κ_{ij} (β_{ij}) represents that transition's fractional contribution to the overall population (depletion) of j (i) by all types of transitions from (to) all levels m.

To determine the critical energy transfer pathways for conferring spectrally pure emission, we selected a transition of interest, $i \rightarrow j$, and examined the transitions that populated i with the highest rates, such that $\sum \kappa_{ij} > 0.8$. We iteratively investigated each of these contributing transitions in the same manner as the original, until the transitions looped back onto themselves or terminated at a ground state.

Table S1. General simulation parameters.

Parameter	***Value***
Simulation time period (ms)	20
Phonon energy (cm^{-1})	450
W^0_{MPR}, zero-phonon relaxation rate(s^{-1})[10]	$1 \cdot 10^7$
α, MPR rate constant(cm)[11]	$3.5 \cdot 10^{-3}$
Index of refraction (β-$NaYF_4$)	1.5
Volume per potential dopant site (nm^3)	$7.2395 \cdot 10^{-2}$
Minimum dopant distance, β-$NaYF_4$ (nm)	0.3867
Absorption fwhm (cm^{-1})	400

Table S2. Judd-Ofelt parameters and reduced matrix elements.

Parameter	***Tm^{3+}***
Ω_2 (10^{-20} cm^2)	2.04
Ω_4	2.01
Ω_6	1.44
Source, Ω_λ	Ivanova *et al* ($Na_{0.4}Y_{0.6}F_{2.2}$:Tm^{3+})[12]
Source, $\lvert\langle i \rvert U^\lambda \rvert j\rangle\rvert^2$	Kaminskii *et al.*[13]

3. Absorption spectra of Tm^{3+}

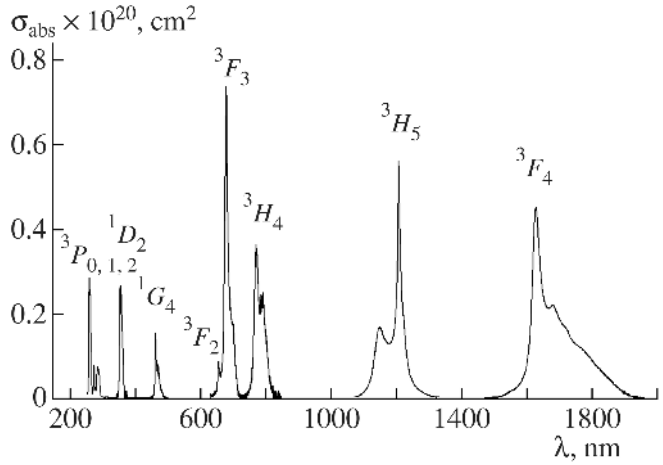

Figure S1. Ground state absorption spectrum of bulk sodium yttrium fluoride doped with Tm^{3+} at 300K. Reproduced with permission from Ivanova et al.[12]

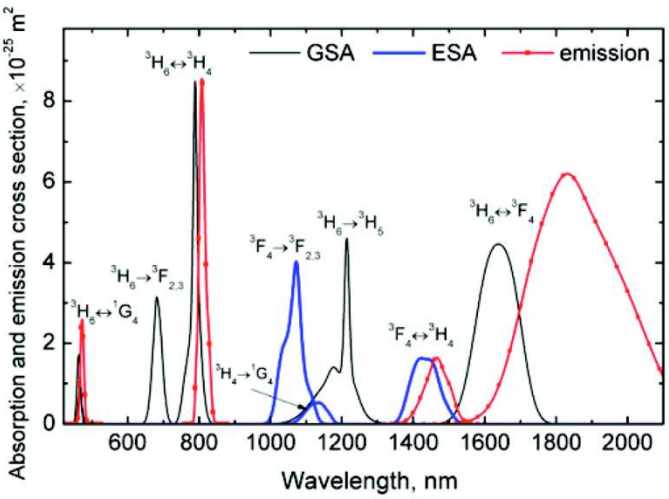

Figure S2. Ground state absorption (black) and excited state absorption (blue) spectra of Tm^{3+}-doped silica fiber at 300K. Reproduced with permission from Peterka et al.[14]

4. Theoretical steady-state populations for Tm^{3+} -doped ELNPs

Steady-state manifold populations calculated for ELNPs doped with 1% Tm^{3+} excited at 1064 nm (10^5 W/cm^2). Populations correspond to the steady-state mechanism shown in Figure 4.

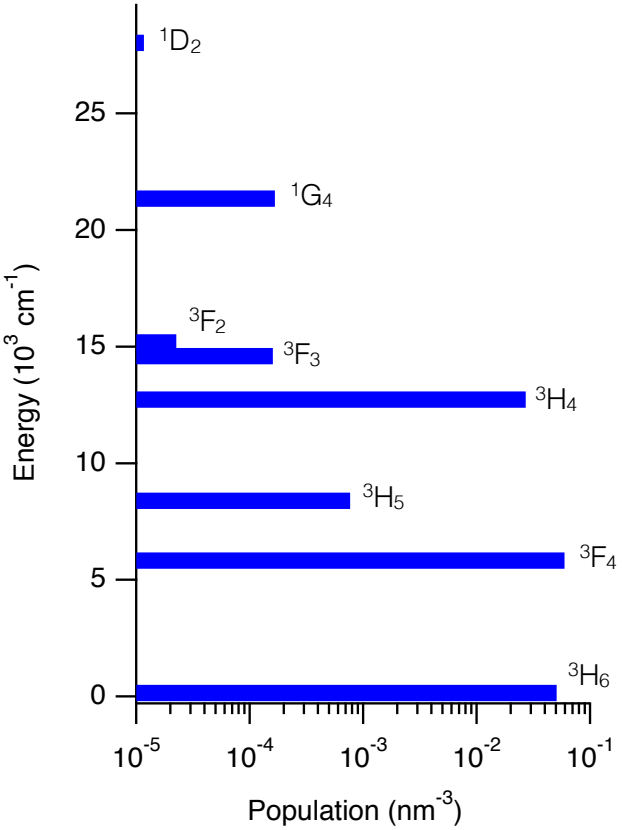

Figure S3. Steady-state manifold populations calculated for ELNPs doped with 1% Tm^{3+}.

Table S3. Steady state populations for $NaYF_4$:Tm^{3+} (1%)

Manifold # (i)	*$^{2S+1}L_J$*	*Energy (cm^{-1})*	*N_i (nm^{-3})*
0 (Ground state)	$^3H_6$	153	5.06E-02
1 (Key intermediate)	$^3F_4$	5828	5.94E-02
2	$^3H_5$	8396	7.66E-04
3 (800-nm emitting)	$^3H_4$	12735	2.70E-02
4	$^3F_3$	14598	1.59E-04
5	$^3F_2$	15180	2.25E-05
6	$^1G_4$	21352	1.67E-04
7	$^1D_2$	28028	1.17E-05

5. Major transitions predicted by theory for Tm^{3+}-doped $NaYF_4$

The following tables list the major transitions and their steady-state rates depicted in the mechanism in Figure 4. Manifold numbers *i* and *j* are enumerated in Table S3. For ET donor (acceptor) transitions, the ET complement transition in parentheses is the acceptor (donor) transition. dNj/dt is the rate of the transition at steady state. β_{ij} and κ_{ij} are branching and contribution ratios, respectively (described in Section 2).

Transition types: ED = electric dipole, MD = magnetic dipole, rad. = radiative emission, abs. = absorption, ET donor (acceptor) = donor (acceptor) transition of energy transfer, MPR = multiphonon relaxation.

Table S4. Major steady state transitions, $NaYF_4$:Tm^{3+} (1%)

Transition type	*Transition i→j (ET complement)*	*dN_j/dt (nm^{-3}/s)*	*β_{ij}*	*κ_{ij}*	*Change in energy (cm^{-1})*
ET acceptor (CR)	**0→1 (3→1)**	**33.6**	**0.838**	**0.279**	**5675 (-6907)**
ED abs. (GSA)	**0→2**	**1.5**	**0.036**	**0.030**	**8243**
ED abs. (ESA)	**1→5**	**77.9**	**0.647**	**0.870**	**9352**
ET acceptor	1→2 (3→2)	14.3	0.119	0.293	2568 (-4339)
ED rad.	1→0	7.5	0.062	0.187	-5675
ET donor	1→0 (1→2)	6.6	0.055	0.165	-5675 (2568)
ET acceptor	1→2 (1→0)	6.6	0.055	0.135	2568 (-5675)
MPR	2→1	37.7	0.771	0.313	-2568
ET donor	**3→1 (0→1)**	**33.6**	**0.346**	**0.279**	**-6907 (5675)**
ED rad.	**3→0**	**21.1**	**0.217**	**0.526**	**-12582**
ET donor	3→2 (1→2)	14.3	0.147	0.293	-4339 (2568)
ET donor	3→2 (3→5)	3.0	0.031	0.062	-4339 (2445)
MPR	3→2	2.7	0.028	0.055	-4339
MPR	4→3	92.5	0.964	0.952	-1863
MPR	5→4	88.7	0.991	0.924	-582

6. Quantum yield calculations

Calculation of quantum yields. Theoretical quantum yields for the Tm^{3+} $^3H_4 \rightarrow {}^3H_6$ transition were calculated by dividing the overall photon emission rate (e.g., dN_j/dt values in Table S4), integrated from 700 to 900 nm, by the absorption rate of 1064 nm photons.

Simulation of surface species. To simulate the effect of non-radiative surface quenching sites in nanocrystals, we introduced a surface species into our model using a previously reported method.[15] To simulate the vibrational modes of surface ligands and other processes that could non-radiatively relax the excited states of lanthanide ions near the surface of the nanocrystals, the surface species were given excited states with energies that correspond to vibrational modes of bonds found in typical organic ligands. The energy transfer is dependent on the line strengths S of ground state absorption transitions to the surface species' excited states. For all ground state transitions, we estimated line strength S values of $5 \cdot 10^{-21}$ cm^2 based on typical integrated molar absorptivities of organic molecules of 100-50,000 $M^{-1}cm^{-2}$ (see, for example, sodium oleate[16] at ~3000 cm^{-1}). Surface species that accept energy from lanthanide species rapidly relax in energy via non-radiative pathways.

Because resonant donor-to-donor energy migration enables rapid energy transfer across large distances in highly doped materials, it was not necessary for our model to distinguish between lanthanide ions adjacent to surface states and those far away. Our model accounted for the size of nanoparticles by varying the concentration of the "surface" states according to the surface-area-to-volume ratio of the nanocrystals, assuming a surface defect state for every ligand on the surface of a nanoparticle, with an approximate value of one ligand or surface state per nm^2 surface area[17]. For an 8-nm particle with surface area SA = 201 nm^2 and volume V = 268 nm^3 there would be 0.75 surface states/nm^3. We have 13.8 dopant sites/nm^3, so 0.75/13.8 = 0.054 surface species per available dopant site in an $NaYF_4$ nanocrystal, or effectively 5 mol % of surface species in the nanocrystal.

Table S5. Calculated quantum yields $NaYF_4:Tm^{3+}$ emission (700-900 nm) under 1064 nm excitation

Diameter (nm)	*Composition (Tm %)*	*% Surface species*	*Quantum Yield (%) @ 10^5 W/cm^2*
Bulk, or thick shell	1.5	0	19.8
11	1.5	4	0.0702
8	0.5	5	0.0404
8	1	5	0.0455
8	1.5	5	0.0464
8	2	5	0.0461
8	4	5	0.0423
8	10	5	0.0345
8	20	5	0.0357

7. TEM and XRD characterization

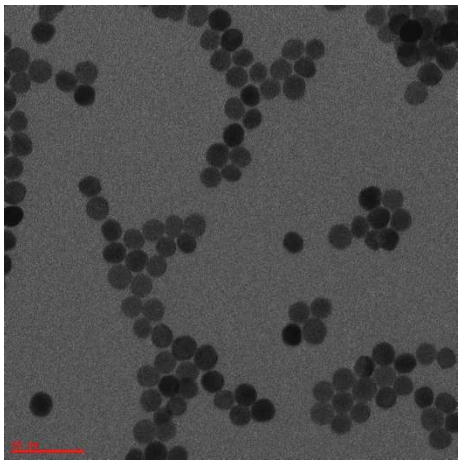

Figure S4. Transmission electron micrographs of representative $NaYF_4$: 20% Gd^{3+}, 0.5% Tm^{3+}@$NaGdF_4$ core-shell nanocrystals with diameter d= 15 ± 1 nm. Scale bar = 50 nm.

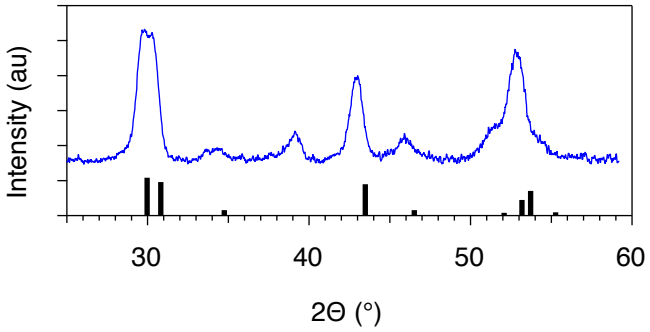

Figure S5. Representative X-ray diffraction spectra for $NaYF_4$: 20% Gd^{3+}, 0.5% Tm^{3+}@$NaGdF_4$ nanocrystals. Vertical bars correspond to the diffraction peaks for hexagonal β-$NaYF_4$, JCPDS file no. 28-1192.

8. Dynamic light scattering (DLS) of ligand-stripped ELNPs

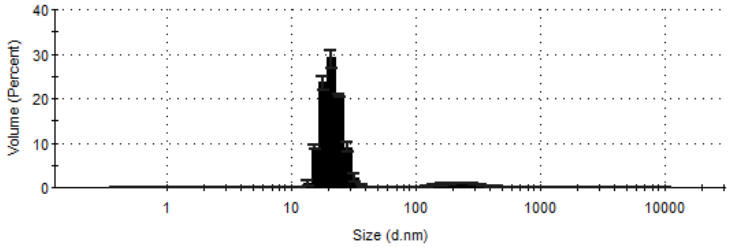

Figure S6. Size histogram of ligand-stripped ELNPs suspended in water, as measured with dynamic light scattering. Nanoparticles were 11-nm $NaYF_4$:20% Gd^{3+}, 1.5% Tm^{3+} cores coated with a 2-nm $NaGdF_4$ shell.

9. Vehicle control for HeLa cell imaging

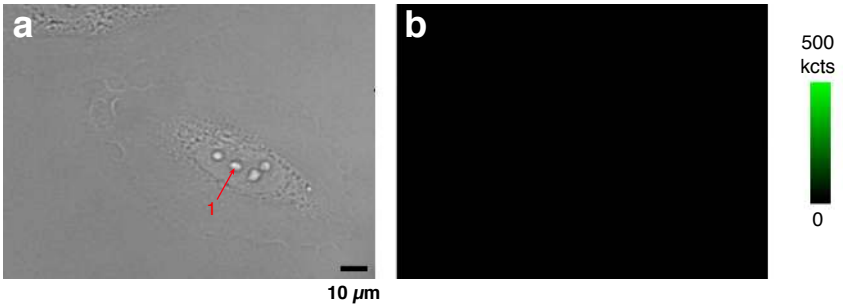

Figure S7. Vehicle control for HeLa cell imaging. (a) Bright-field micrograph of HeLa cell imaged after treatment with no ELNPs but otherwise identical reagents as cells in Figure 5 in the main text. Point 1 indicates the position of the "Control" spectrum shown in Figure 5d. (b) Confocal upconversion luminescence micrograph illustrating the lack of autofluorescence of the unlabeled HeLa cells (a) under 1064-nm excitation (10^6 W/cm^2). Emission was integrated between 740 and 870 nm. For comparison, intensities use the same color scale as Figure 5.

10. Cell viability assays

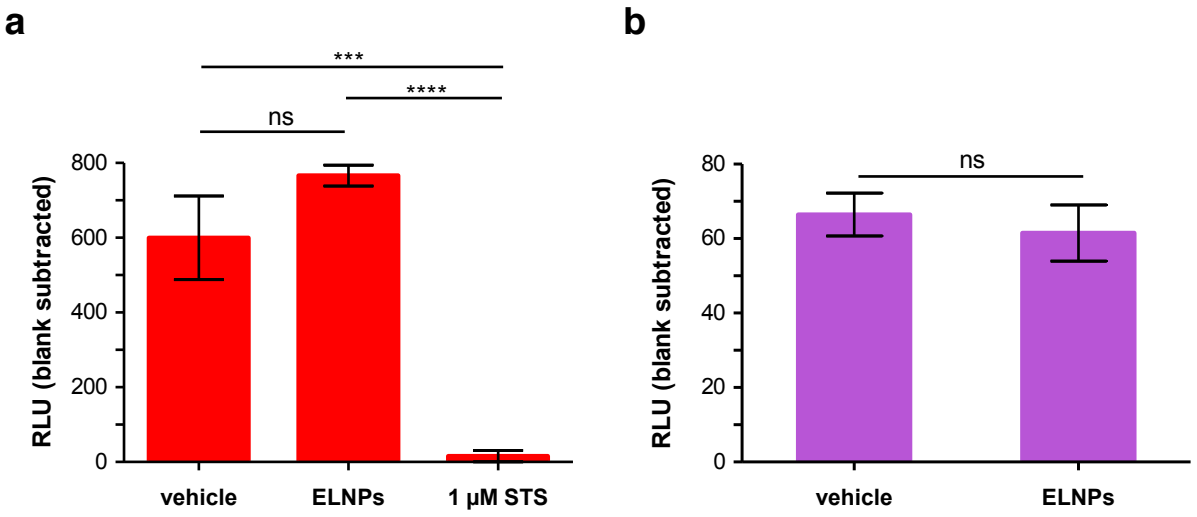

Figure S8. ELNP-treated HeLa cells are viable following a 17 h incubation. (a) CellTiter-Glo assay demonstrating that ELNP and vehicle-treated cells are equally viable in comparison to cells given an apoptotic inducer, staurosporine[18] (STS). P values: ns = 0.0662, *** = 0.0009, **** = 0.0001. (b) ELNPs do not contribute toward any signal interference in the CellTiter-Glo assay as compared to vehicle. No cells were included in this assay. P value: ns = 0.6303.

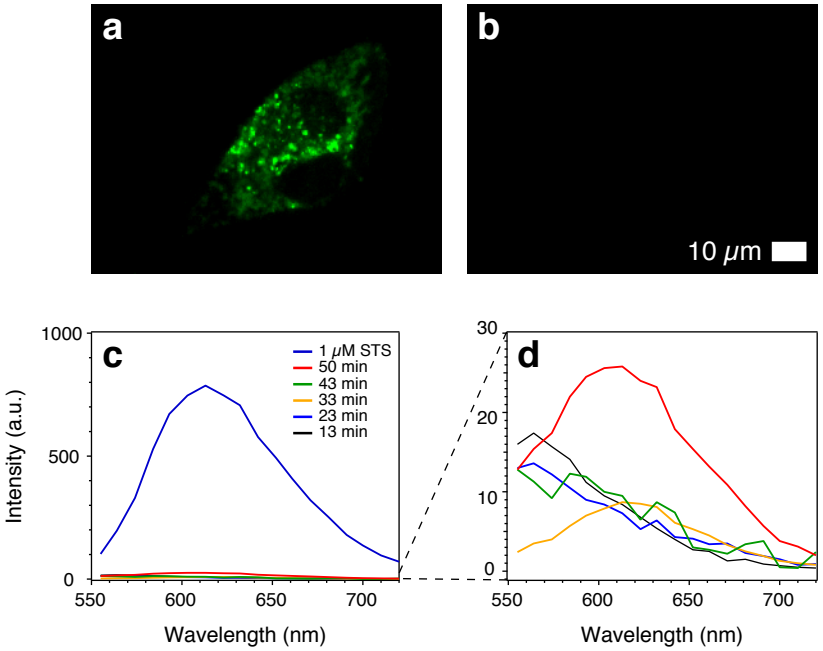

Figure S9. HeLa cells after 23 min of imaging at 1064 nm radiation at 10^6 W/cm^2. Cell corresponds to the cell imaged in Figure 6. (a) Autofluorescence under 488-nm excitation. (b) Propidium iodide emission micrograph under 514 nm excitation. (c) Propidium iodide emission spectra from live HeLa cells exposed to 1064 nm over five different durations, or to 1 μM STS (positive control). Spectra were extracted from region occupying cell of interest. Values were background subtracted using identically sized region in field of view without cells. (d) Magnified spectra from (c) highlighting the emergence of PI staining at 50 min exposure, indicating cell death.

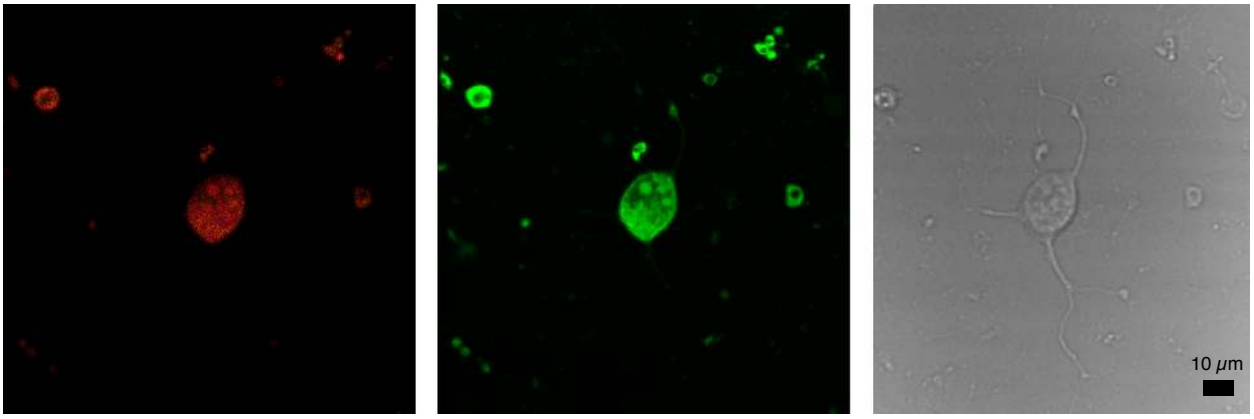

Figure S10. (a) Staurosporine-treated HeLa cells excited at 514 nm show positive staining for propidium iodide (PI), indicating cell death. Cellular autofluorescence (b) and bright-field (c) micrographs were collected as a reference to PI staining.

11. Confocal imaging through phantoms and mouse brain

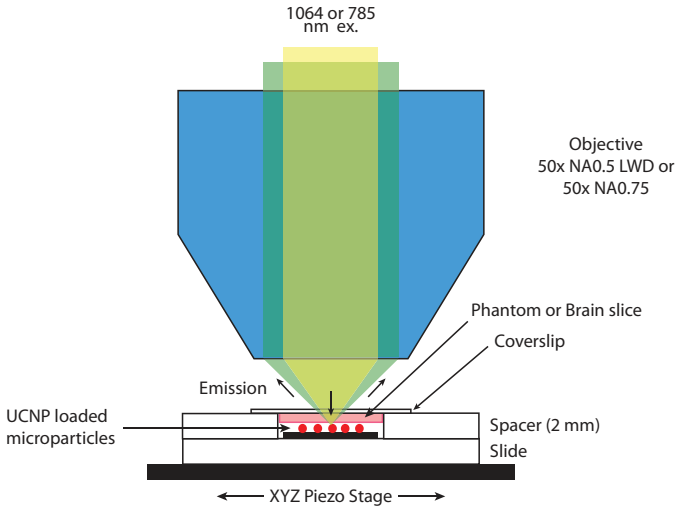

Figure S11. Microscope setup for imaging phantoms and brain slices.

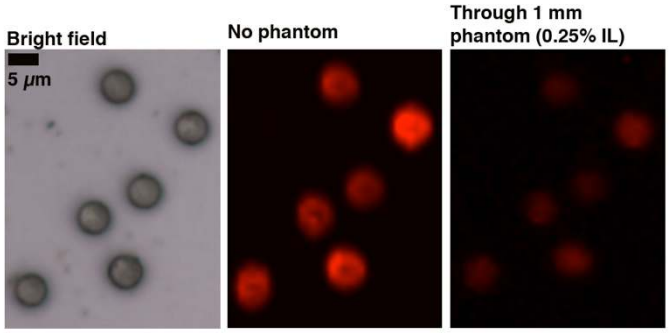

Figure S12. PS beads with $NaYF_4$: Gd^{3+},Nd^{3+},Yb^{3+},Ho^{3+} (20/20/10/2%) UCNPs imaged through 1 mm phantom (0.25% IL), excited at 785 nm and emission integrated over 625-675 nm.

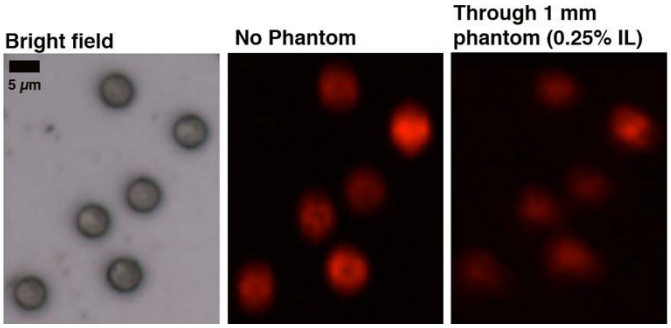

Figure S13. PS beads with $NaYF_4$: Gd^{3+},Nd^{3+},Yb^{3+},Ho^{3+} (20/20/10/2%) UCNPs imaged through 1 mm phantom (0.25%IL), excited at 785 nm and emission integrated over 530-560 nm.

12. Additional mouse brain imaging at 785 nm excitation

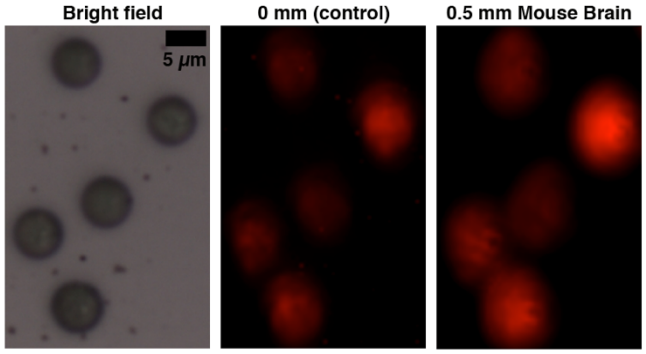

Figure S14. (a) PS beads with $NaYF_4$: Gd^{3+},Nd^{3+},Yb^{3+},Ho^{3+} (20/20/10/2%) imaged through 0.5 mm mouse brain excited at 785 nm and emission integrated over 625-675 nm. Intensities are in arbitrary units.

13. Magnified line cut for Figure 8

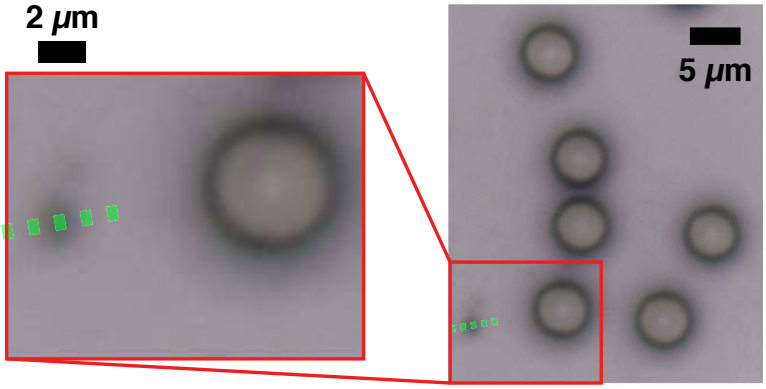

Figure S15. Bright field micrographs of Tm^{3+}- doped ELNP beads showing line (green dashes) along which intensity line cuts were measured for Figure 8c.

14. References

(1) Ostrowski, A. D.; Chan, E. M.; Gargas, D. J.; Katz, E. M.; Han, G.; Schuck, P. J.; Milliron, D. J.; Cohen, B. E. Controlled Synthesis and Single-Particle Imaging of Bright, Sub-10 Nm Lanthanide-Doped Upconverting Nanocrystals. *ACS Nano* **2012**, *6*, 2686–2692.

(2) Chan, E. M.; Xu, C.; Mao, A. W.; Han, G.; Owen, J. S.; Cohen, B. E.; Milliron, D. J. Reproducible, High-Throughput Synthesis of Colloidal Nanocrystals for Optimization in Multidimensional Parameter Space. *Nano Lett.* **2010**, *10*, 1874–1885.

(3) Li, X.; Shen, D.; Yang, J.; Yao, C.; Che, R.; Zhang, F.; Zhao, D. Successive Layer-by-Layer Strategy for Multi-Shell Epitaxial Growth: Shell Thickness and Doping Position Dependence in Upconverting Optical Properties. *Chem. Mater.* **2013**, *25*, 106–112.

(4) Mehra, S.; Chan, E. M.; Salleo, A. Modular Synthetic Design Enables Precise Control of Shape and Doping in Colloidal Zinc Oxide Nanorods. *J. Mater. Chem. C* **2015**, *3*, 7172–7179.

(5) Han, M.; Gao, X.; Su, J. Z.; Nie, S. Quantum-Dot-Tagged Microbeads for Multiplexed Optical Coding of Biomolecules. *Nat. Biotechnol.* **2001**, *19*, 631–635.

(6) Bogdan, N.; Vetrone, F.; Ozin, G. A.; Capobianco, J. A. Synthesis of Ligand-Free Colloidally Stable Water Dispersible Brightly Luminescent Lanthanide-Doped Upconverting Nanoparticles. *Nano Lett.* **2011**, *11*, 835–840.

(7) Gee, S.; Ellwood, I.; Patel, T.; Luongo, F.; Deisseroth, K.; Sohal, V. S. Synaptic Activity Unmasks Dopamine D2 Receptor Modulation of a Specific Class of Layer v Pyramidal Neurons in Prefrontal Cortex. *J. Neurosci.* **2012**, *32*, 4959–4971.

(8) Chan, E. M.; Gargas, D. J.; Schuck, P. J.; Milliron, D. J. Concentrating and Recycling Energy in Lanthanide Codopants for Efficient and Spectrally Pure Emission: the Case of NaYF4:Er3+/Tm3+ Upconverting Nanocrystals. *J. Phys. Chem. B* **2012**, *116*, 10561–10570.

(9) Chan, E. M. Combinatorial Approaches for Developing Upconverting Nanomaterials: High-Throughput Screening, Modeling, and Applications. *Chem. Soc. Rev.* **2015**, *44*, 1653–1679.

(10) van Dijk, J. M. F.; Schuurmans, M. F. H. On the Nonradiative and Radiative Decay-Rates and a Modified Exponential Energy-Gap Law for 4f-4f Transitions in Rare-Earth Ions. *J. Chem. Phys.* **1983**, *78*, 5317–5323.

(11) Miyakawa, T.; Dexter, D. Phonon Sidebands, Multiphonon Relaxation of Excited States, and Phonon-Assisted Energy Transfer Between Ions in Solids. *Phys. Rev. B* **1970**, *1*, 2961–2969.

(12) Ivanova, S. E.; Tkachuk, A. M.; Mirzaeva, A.; Pelle, F. Spectroscopic Study of Thulium-Activated Double Sodium Yttrium Fluoride Na0.4Y0.6F2.2 : Tm3+ Crystals: I. Intensity of Spectra and Luminescence Kinetics. *Opt. Spectrosc.* **2008**, *105*, 228–241.

(13) Kaminskii, A. A. *Crystalline Lasers*; CRC Press: Boca Raton, FL, 1996.

(14) Peterka, P.; Kasik, I.; Dhar, A.; Dussardier, B.; Blanc, W. Theoretical Modeling of Fiber Laser at 810 Nm Based on Thulium-Doped Silica Fibers with Enhanced 3H4

Level Lifetime. *Opt. Express* **2011**, *19*, 2773–2781.
(15) Gargas, D. J.; Chan, E. M.; Ostrowski, A. D.; Aloni, S.; Altoe, M. V. P.; Barnard, E. S.; Sanii, B.; Urban, J. J.; Milliron, D. J.; Cohen, B. E.; *et al.* Engineering Bright Sub-10-Nm Upconverting Nanocrystals for Single-Molecule Imaging. *Nat. Nanotechnol.* **2014**, *9*, 300–305.
(16) Kellar, J. J.; Cross, W. M.; Miller, J. D. *Adsorption Density Calculations From In Situ FT-IR/IRS Data at Dilute Surfactant Concentrations*; Appl. Spectrosc., 1989; Vol. 43, pp 1456–1459.
(17) Gomes, R.; Hassinen, A.; Szczygiel, A.; Zhao, Q.; Vantomme, A.; Martins, J. C.; Hens, Z. Binding of Phosphonic Acids to CdSe Quantum Dots: a Solution NMR Study. *J. Phys. Chem. Lett.* **2011**, *2*, 145–152.
(18) Wolan, D. W.; Zorn, J. A.; Gray, D. C.; Wells, J. A. Small-Molecule Activators of a Proenzyme. *Science* **2009**, *326*, 853–858.